Prompt neutrons in correlation with fission fragments from ^{235}U(n, f)

Alf Göök,* Franz-Josef Hambsch, Stephan Oberstedt, and Marzio Vidali
European Commission - Joint Research Centre, Directorate G, Retieseweg 111, B-2440 Geel, Belgium

(Received 23 March 2018; revised manuscript received 5 June 2018; published 18 October 2018)

Improved knowledge of prompt emission in fission has significant implications for our understanding of the fission process. It is also important for improving nuclear data evaluation, with impact on applications. The correlation between prompt neutrons and fragments emitted in binary neutron induced fission of ^{235}U has been studied at the GELINA facility. The experiment employs an array of proton recoil scintillators and a position-sensitive twin ionization chamber. This experimental arrangement permits measurement of the correlations between neutron emission, fragment angle, and mass and energy of the fission fragments. In this article, we present results on prompt fission neutron energy and multiplicity correlations with mass and total kinetic energy of the fission fragments. Results from the present measurement shows distinct differences compared to earlier studies of the correlated fission fragment and prompt neutron emission quantities. The differences with respect to earlier investigations are interpreted as improved fission fragment energy resolution in the present measurement. The present result supports several recent model calculations of prompt neutron and fission fragment correlations.

DOI: 10.1103/PhysRevC.98.044615

I. INTRODUCTION

In fission, primary fragments release excitation energy by the emission of neutrons and γ rays. Improved knowledge of the properties of the prompt fission neutrons (PFN), their multiplicities, as well as their energy and angular distributions can shed light on the fission process near the scission point. These properties are related to the deformation of fission fragments at scission, the sharing of excitation energy between the fragments, and the timescale of the process itself. In recent years large efforts have been put into the modeling of PFN emission in fission [1–7]. From an application perspective, one of the major driving forces behind these efforts is to develop tools for improved evaluations of nuclear data on prompt fission neutron spectra (PFNS), in neutron-induced fission [8]. For many applications in nuclear science and technology the PFNS plays an important role. Specifically, for accurate prediction of nuclear criticality with neutron transport codes the PFNS can significantly impact the results. A second major driving force has been to develop realistic correlated fission neutron sources, in terms of energy and angular distributions, for Monte Carlo transport codes. This has strong impact on, for example, nonproliferation and nuclear safeguards applications [9]. The efforts to model PFN emission in fission have been quite successful in both consistency among different approaches and reproducing available experimental data. However, in the case of ^{235}U(n, f) difficulties have been encountered [10,11], specifically in modeling the dependence of the average number of neutrons emitted per fission $\overline{\nu}$ on the fragment total kinetic energy (TKE). Possible deficiencies in the available experimental data have been pointed out by Kornilov *et al.* [11]. Correlated PFN and fission fragment data are used in the development of the models to verify theoretical assumptions, as well as to tune model parameters [1,2]. As the available data might be disputable and the models require accurate experimental data, it is of importance to revisit PFN correlations with fission fragment properties in ^{235}U(n, f) experimentally.

Experimental investigations of prompt fission neutrons and fission fragment properties in resonance neutron induced fission on ^{235}U have been performed at the GELINA facility of the Joint Research Centre, Geel, Belgium (JRC-Geel). In this article, we present results on PFN correlations with fission fragments extracted from the data by summing over the incident neutron energy range [0.26 eV, 45 keV].

II. EXPERIMENT

The method used to study PFN and fission fragment correlations is based on techniques pioneered by Bowman *et al.* [12]. Empirically, it has been observed that the bulk of neutrons are emitted from the fragments after full acceleration [12–15]. By measurement of the relevant kinematic parameters in the laboratory frame, the emission process in the rest frame of the fully accelerated fragments (from here on referred to as the c.m. frame) can be reconstructed on an event-wise basis.

The experiment has been performed at the GELINA neutron time-of-flight facility. The detector setup, schematically illustrated in Fig 1, consists of two parts: an array of proton recoil scintillators (SCINTIA) and a twin position-sensitive

*alf.gook@ec.europa.eu

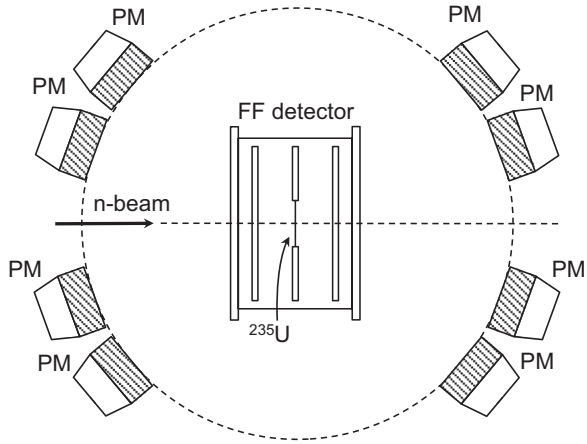

FIG. 1. Schematic view of the experimental arrangement. The ^{235}U target is placed in the center of the fission fragment detector, which is surrounded by the array of neutron detectors (denoted PM).

ionization chamber for fission fragments. More details about the detector setup are given below. The data acquisition is based on wave-form digitizers. A pulse from the common cathode of the twin ionization chamber triggers the data acquisition to store digital wave forms from all ionization chamber electrodes and scintillation detectors on disk for offline analysis. Together with the wave-form data, 800 MHz time-stamp information is also written. A signal from GELINA generated just before an electron pulse hits the neutron producing target is used to reset the time stamp, allowing the incident neutron energy to be determined via the time-of-flight technique. The main experiment was performed with GELINA operating at 800 Hz repetition frequency. With the incident neutron flight-path length of 8.81 m, the lowest neutron energy accessible in this measurement is 0.26 eV. To avoid overlap of low energy neutrons from a former e^--beam pulse, a Cd filter with an areal density of 0.7 g/cm^2 was placed in the beam. The data presented in this paper were obtained by summing over the incident neutron energy range [0.26 eV, 45 keV]. The average energy of the neutrons inducing fission is 1.16 keV, as determined from the observed time-of-flight spectrum.

A. Fission fragment detection

The position-sensitive twin ionization chamber is used for determination of fission fragment masses and energies. This detector has been developed at JRC-Geel and is described in detail elsewhere [16], only some crucial details will be repeated here. The detector is essentially a twin Frisch gridded ionization chamber, but with the standard anode plates replaced by position sensing readout electrodes. A thin layer (67.2 μg/cm^2) of $^{235}UF_4$ on a backing of 27 μg/cm^2 polyimide covered by 50 μg/cm^2 gold is placed in a hole in the central cathode. The target and backing are thin enough that both fission fragments from a binary event can escape and ionize the gas on either side of the cathode plate.

Fission fragment energies and masses are determined via the double-kinetic-energy ($2E$) technique. For the purpose of calibration, data collected with GELINA operating at 50 Hz repetition frequency and selecting incident neutron energies in the range [0.16 meV, 0.17 eV] have been used; during this run the Cd filter was removed from the beam. As counting gas the P-10 gas mixture was used. The pulse height defect of the counting gas is corrected for as in Ref. [17], with parameters adjusted to reproduce known values of the average light and heavy fragment masses [18] and TKE [19] from ^{235}U($n_{\rm th}$, f). The masses $m^*_{1,2}$ and energies $E^*_{1,2}$ before neutron emission in a binary fission event are related via conservation of linear momentum, according to

$$m^*_{1,2} = m_{cn}\frac{E^*_{2,1}}{E^*_1 + E^*_2}, \quad (1)$$

where m_{cn} is the mass of the compound nucleus undergoing fission. Under the assumption of isotropic neutron emission from fully accelerated fragments, the energies before neutron emission E^* are related to the energies after neutron emission E by the approximation

$$E^* = E\frac{m^*}{m^* - \overline{\nu}(m^*, \mathrm{TKE})}, \quad (2)$$

where $\overline{\nu}$ is the number of neutrons emitted by the fragment. The dependence of $\overline{\nu}$ on mass and TKE can only be derived from the data once the $2E$ analysis is completed. As initial assumption we have used the evaluated data on $\overline{\nu}(m^*)$ from Wahl [20] and the parametrization

$$\overline{\nu}(m^*, \mathrm{TKE}) = \overline{\nu}(m^*) + \frac{\overline{\nu}(m^*)}{\overline{\nu}(m^*) + \overline{\nu}(m_{cn} - m^*)}\Delta_{\mathrm{TKE}}, \quad (3)$$

where

$$\Delta_{\mathrm{TKE}} = \frac{\overline{\mathrm{TKE}}(m^*) - \mathrm{TKE}}{E_{\mathrm{sep}}}, \quad (4)$$

where $E_{\mathrm{sep}} = 8.6$ MeV/n is the average energy necessary to emit a neutron [21]. The analysis was later repeated using the results for $\overline{\nu}(m^*)$ and $E_{\mathrm{sep}} = 8.51$ MeV/n derived from the data. No significant changes in the results were observed between the two analyses, hence no further iteration was made. For the case when a neutron coincidence is required, an additional correction to the fragment energy according to Ref. [22] is applied.

The intrinsic energy resolution of the ionization chamber is for fission fragments $\lesssim$0.6 MeV [14]. However, the finite target thickness causes an uncertainty in the energy loss correction that dominates the resolution for the individual fragments, since the depth inside the target where the fission took place is unknown. This uncertainty is on average about 1.5 MeV, as determined from the observed energy loss in the target material. In addition to the resolution of the measured energies, conversion of the measured post-neutron energies to pre-neutron energies, relevant for calculating the fission fragment masses, adds broadening. The resolution due to neutron emission can be estimated according to Ref. [23]. Combined an average mass resolution of about 5 u (FWHM) is expected. In order to verify this expectation, the mass distribution selecting only thermal incident neutron energies from the present measurement was compared to high resolution data from Ref. [18], as displayed in Fig. 2. The red dashed line corresponds to the data of Ref. [18]

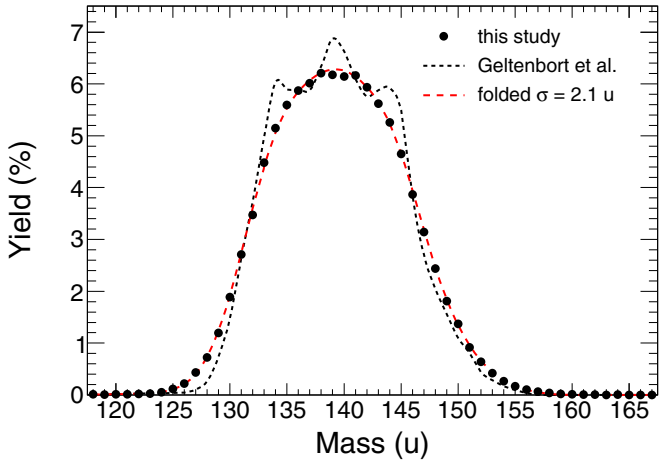

FIG. 2. Comparison of the pre-neutron fragment mass distribution from thermal neutron induced fission observed in this work (black circles) with the one observed in Ref. [18] (dashed black line). The red dashed line is the result of convolution of the data of Ref. [18] with the mass resolution (4.9 u FWHM) of this work.

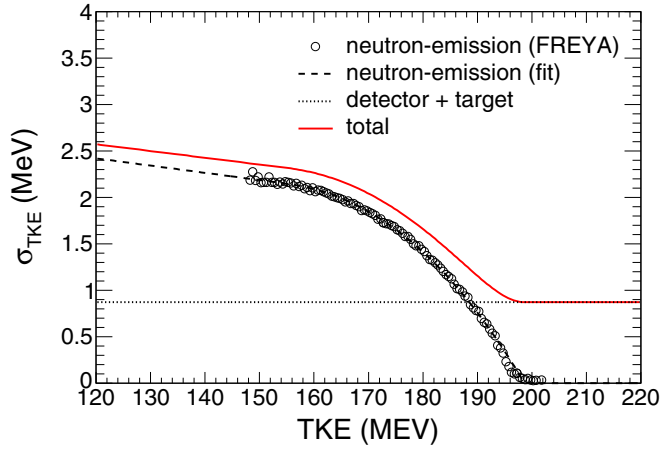

FIG. 3. Calculated pre-neutron TKE resolution due to neutron emission (open circles), using the fission event generator FREYA [5,6]. The dashed line represents a polynomial fit to the simulated data, with a linear extrapolation below 150 MeV. The dotted line represents the effect of energy loss in the target and intrinsic energy resolution of the ionization chamber. The full red line represents the sum of the effects.

convoluted with a Gaussian resolution function; the best fit for the FWHM of this resolution function was found to be 4.9 u.

The resolution in TKE due to the target thickness was estimated to 0.2 MeV, based on energy loss calculations of typical fission fragments using TRIM [24]. The reason that this is significantly smaller than the resolution that applies to the individual fragments is that the uncertainty on the depth inside the target where the fission takes place cancels to a large extent. Adding the intrinsic resolution, the post-neutron TKE resolution is then estimated to be 0.9 MeV. As for the individual energies, conversion of the measured post-neutron energies to pre-neutron energies adds broadening to the TKE. This broadening depends on the number of neutrons emitted and the width of the neutron emission probability around the average $\overline{\nu}(m^*, \mathrm{TKE})$. The effect of TKE broadening due to neutron emission was estimated by a Monte Carlo calculation using the fission event generator FREYA [5,6]. The result is displayed in Fig. 3, which shows the standard deviation of the pre-neutron TKE about the average. The average TKE is obtained by correcting the post-neutron energies according to Eq. (2), as in the experimental data analysis.

The orientation of the fission axis is determined from combined information on the electron drift time and charge division from the position electrodes. This gives the position of the center of gravity of the charge distribution along the stopping tracks of both fission fragments individually. By connecting these two points by a straight line, the position of the fission event on the target plane as well as the orientation of the fission axis is extracted, with resolutions of 1.5 mm (FWHM) and 7° (FWHM), respectively. This information is then used to determine the relative orientation of the fission fragment velocity and the velocity of a neutron detected in any of the scintillators. A more detailed account of this analysis can be found in Ref. [16].

The ionization chamber covers nearly 4π of the solid angle. However, due to energy straggling and uncertainty in the energy loss corrections, fission fragment masses cannot be accurately determined for angles of emission larger than 60° with respect to the target normal. The collimation is done during the offline data analysis by imposing a cutoff angle using the information extracted on the fission axis orientation. The cutoff angle causes a fission fragment efficiency that varies as a function of angle relative to a specific neutron detector ϑ_L. By counting the number of fissions as a function of ϑ_L (regardless of whether a neutron has been registered in coincidence or not) the fission fragment efficiencies are determined and accounted for; cf. Ref. [16].

B. Prompt neutron detection

An array of proton recoil scintillators was used to detect prompt fission neutrons. In Table I properties of the neutron detectors and their position relative to the center of the fission target inside the ionization chamber are summarized. The PFN energy is determined from the flight time of the neutrons from the ionization chamber to the scintillation detector. A typical time-of-flight spectrum is displayed in Fig. 4. The energy resolution is given by the combination of uncertainty in the flight time and the flight-path length, due to the size of the detectors (as given in Table I). The combined timing resolution of the ionization chamber and the scintillation detectors is dominated by the ionization chamber, and has been determined to be 1.1 ns (FWHM). The selection of prompt fission neutrons is made using pulse-shape discrimination (PSD) and pulse-height thresholds. In addition to neutrons, fission is accompanied by prompt γ-ray emission. For low energy deposits in the scintillators, PSD fails to distinguish between γ-rays and neutrons, leaving a residual γ-ray component after PSD selection. Most of the prompt γ emission happens at the instant of fission and up to a few ns later [25]. Within the same time range, high-energy neutrons, which are emitted with a very

TABLE I. Summary of the neutron detector array. Three different type of detectors were used; the EJ-301 is an NE-213 equivalent liquid scintillator, while the paratherphenyl (pth) and the stilbene are organic crystal scintillators. The distance from the center of the ^{235}U target to the center of the individual detector is denoted by d. The detector orientation axis is given by the polar θ_d and azimuthal ϕ_d angles with respect to the incident beam direction. The position of the individual detector was determined with an accuracy of 0.2 mm, using a measuring arm.[a] The last column gives the size of the scintillator.

Type	d (cm)	θ_d (deg.)	ϕ_d (deg.)	diameter × height (cm × cm)
stilbene	43.37	134.47	−177.16	8.00 × 5.00
pth	41.04	161.88	−174.20	8.00 × 5.00
pth	41.24	159.78	−4.41	8.00 × 5.00
pth	41.83	133.69	−3.30	8.00 × 5.00
EJ-301	45.65	129.35	88.01	10.16 × 5.10
EJ-301	43.58	161.73	84.27	10.16 × 5.10
EJ-301	43.58	160.96	−86.74	10.16 × 5.10
EJ-301	47.98	47.89	93.09	10.16 × 5.10
EJ-301	43.79	44.86	179.37	10.16 × 5.10
EJ-301	43.32	17.26	177.89	10.16 × 5.10
EJ-301	42.50	16.48	−97.41	10.16 × 5.10
EJ-301	44.93	16.90	100.25	10.16 × 5.10
EJ-301	45.90	18.17	0.18	10.16 × 5.10
EJ-301	45.46	41.74	−1.46	10.16 × 5.10
EJ-301	44.82	151.34	38.79	12.70 × 5.10
EJ-301	46.42	154.85	140.90	12.70 × 5.10
EJ-301	45.37	151.54	−129.30	12.70 × 5.10
EJ-301	45.25	149.55	−50.51	12.70 × 5.10
EJ-301	45.89	27.48	137.85	12.70 × 5.10
EJ-301	44.68	28.14	−136.51	12.70 × 5.10
EJ-301	45.47	24.78	−48.97	12.70 × 5.10
EJ-301	44.06	26.29	45.60	12.70 × 5.10

[a]ROMER Absolute Arm 7530, Hexagon Metrology: http://www.hexagonmi.com/en-US/products/portable-measuring-arms/romer-absolute-arm

low intensity, will arrive in the detectors. Therefore, the very high-energy region of the neutron spectrum is most sensitive to false events induced by γ rays. In order to reduce the effect of such false events, the pulse-height threshold is made to depend on the time of flight. The rate of background events caused by interactions of the neutron beam with the experimental environment, as well as ambient background, was determined by counting, as a function of the pulse height threshold, the number of accidental coincidences before the prompt γ-ray peak, in the time-of-flight interval $[-500, -10]$ ns.

1. Determination of the PFNS

The present experiment is not a dedicated PFNS measurement. In order to facilitate the detection efficiency a relatively short flight path for outgoing neutrons was chosen. This compromises the energy resolution, which in turn degrades the accuracy of the determined PFNS. However, because of the importance to nuclear data the results on the PFNS from this experiment have been evaluated in some detail. The PFNS in the ^{235}U reaction has been determined as a ratio to the PFNS

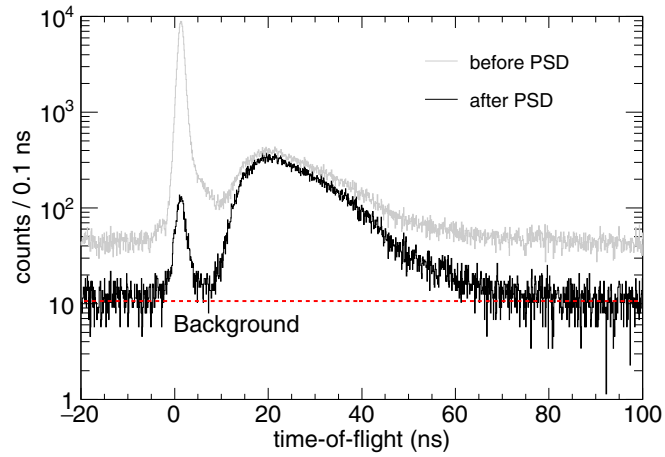

FIG. 4. Time-of-flight spectrum from one of the detectors in the SCINTIA array, before (gray line) and after pulse-shape discrimination has been applied. The red dashed line indicates the estimated background in the scintillator.

from the spontaneous fission of ^{252}Cf. For this purpose the ^{235}U target inside the ionization chamber was replaced by a ^{252}Cf source. The ^{252}Cf source was deposited on a thin (220 μg/cm^2) Ni foil, and had an activity of about 3300 fissions/s. The ^{252}Cf measurement was performed under the same experimental conditions, except for the incident neutron beam which was not present. When determining the PFNS no selection of fission fragment emission angle is made. In fact, for this purpose only the signal from the ionization chamber's central cathode is used as a fission trigger, with a threshold adjusted to discriminate against α decay. Based on the very thin targets, we assume that the PFNS is unperturbed by this selection.

Effects such as multiple scattering of neutrons in the experimental environment and energy resolution alter the shape of the experimentally observed PFNS compared to the true spectrum shape. After conversion of the time of flight to apparent energy E and correction for background, the observed apparent energy spectrum $O(E)$ can be expressed as

$$O(E) = \int \Phi(E')h(E', E)dE', \tag{5}$$

where E' is the true neutron energy, $\Phi(E')$ is the true PFNS, and $h(E', E)$ is a response function. Determination of the PFNS shape $\Phi(E')$ from the experimental time of flight data is a deconvolution problem. A commonly used method for deconvolution is Gold's algorithm [26]. This iterative procedure starts from a guess spectrum shape $\Phi_0(E')$; in each iterative step i the current guess spectrum $\Phi_i(E')$ is convoluted with the response function $h(E', E)$, and a new guess spectrum $\Phi_{i+1}(E')$ is obtained from the ratio

$$\Phi_{i+1}(E) = O(E)\frac{\Phi_i(E)}{\int \Phi_i(E')h(E', E)dE'}. \tag{6}$$

The iterative process continues until the convoluted guess spectrum is in satisfactory agreement with the apparent spectrum.

The response function $h(E', E)$ was calculated using a GEANT4 [27] Monte Carlo code for each detector individually.

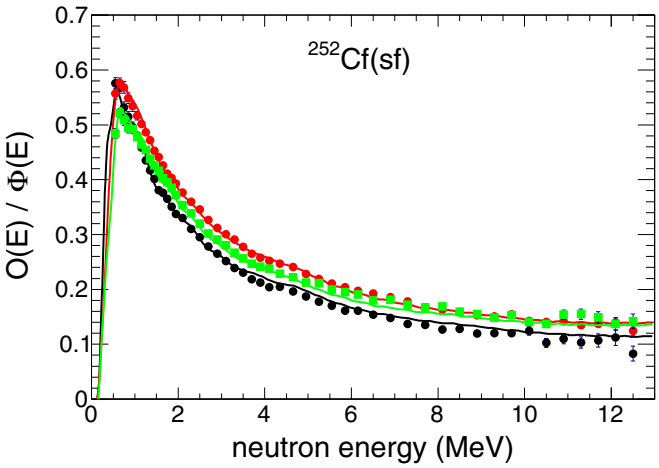

FIG. 5. Neutron detector responses to the ^{252}Cf(sf) PFNS. Differently colored points are experimental while the full lines of the corresponding colors are Monte Carlo calculations of the responses based on the ENDF/B.VII-1 spectrum.

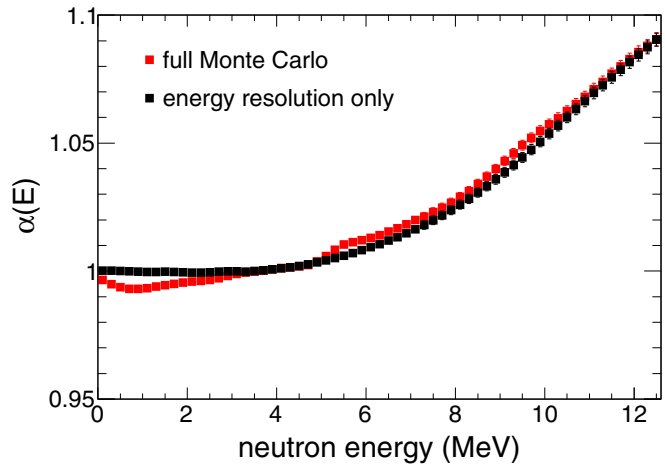

FIG. 6. Calculated correction $\alpha(E)$ for neutron spectrum distortion to the ^{252}Cf(sf)–^{235}U(n, f) PFNS ratio. The red (gray) points represent the applied correction calculated from the full Monte Carlo model of the setup (see text for details), while black points represent a Monte Carlo calculation based on timing and flight path resolution only.

The Monte Carlo code incorporates materials surrounding the fission source and the neutron detectors, including the ionization chamber, the frame holding the neutron detectors, and the concrete floor in order to model scattering and absorption. The Monte Carlo code also models the neutron detection efficiency. In order to do so the pulse-height response for different recoil particle species is needed. The pulse-height response is due to scintillation light production and collection efficiency, and is commonly referred to as the light output. These properties tend to vary slightly from detector to detector, even of the same type. Therefore, each of the detectors has been separately characterized in terms of the recoil proton light-output relative to Compton scattered electrons. The method and setup for the characterization are the same as in Ref. [28]. For recoil particles other than protons, literature data [29,30] scaled with the relative proton light-output, are used in the code. In addition to serving as the basis for the PFNS ratio determination, the measurement performed with the ^{252}Cf source serves as a validation of the Monte Carlo model. As an example of this validation, Fig. 5 shows a comparison of experimental and simulated responses for three of the detectors in the array. The ordinate is the apparent energy from time of flight, while the abscissa shows the ratio between the observed spectrum and the ^{252}Cf(sf) spectrum from ENDF/B.VII-1.

For the ^{252}Cf(sf) PFNS we use the ENDF/B.VII-1 spectrum as the initial guess. Since the ^{252}Cf(sf) PFNS is a standard, we consider the spectrum shape as known, and no further iteration is done to alter this guess spectrum. Agreement between the convoluted guess spectrum and the experimental apparent spectrum was observed within ±3%.

For the ^{235}U(n, f) spectrum the evaluated thermal neutron induced PFNS in Ref. [31] was used as the initial guess spectrum. The spectrum obtained after a single iteration agrees within the experimental uncertainty with the input spectrum, hence no further iterative step is done for this spectrum either. The spectrum ratio corrected for multiple scattering and energy resolution may then be written as

$$R(E) = \frac{O_{\mathrm{Cf}}(E)}{O_{\mathrm{U}}(E)}\,\alpha(E), \tag{7}$$

where

$$\alpha(E) = \frac{\Phi_{\mathrm{Cf}}(E)}{\Phi_{\mathrm{U}}(E)}\,\frac{\int \Phi_{\mathrm{U}}(E')h(E', E)dE'}{\int \Phi_{\mathrm{Cf}}(E')h(E', E)dE'}, \tag{8}$$

and $\Phi_{\mathrm{Cf,U}}(E)$ are the initial guess spectra for ^{252}Cf(sf) and ^{235}U(n, f), respectively. In Fig. 6 the correction $\alpha(E)$ averaged over all detectors is shown together with a correction that only takes the energy resolution effect into account. It is found that the main distortion of the spectrum is due to the energy resolution.

C. Analysis of fission fragment and prompt neutron coincidences

For the purpose of studying correlations between neutrons and fission fragments it is necessary to know the neutron detection efficiency. It was determined as the ratio between the observed ^{252}Cf spectrum and the ENDF/B.VII-1 spectrum, as exemplified in Fig. 5.

In principle, a neutron detected in coincidence with fission may originate from either of the two fragments. However, due to the kinematic boost, the probability that the neutron originate from the fragment detected in the same hemisphere as where the neutron detector is located is much higher [14]. The data analysis is first made assuming that the probability to detect a neutron from the complementary fragment is zero. With the kinematic information obtained in the laboratory reference frame, the kinematics in the c.m. frame can then be reconstructed. Once the neutron spectrum in the c.m. frame has been obtained the contribution from the complementary fragment may be estimated and subtracted. This is the same procedure as in Refs. [14,32]; the only difference is that here

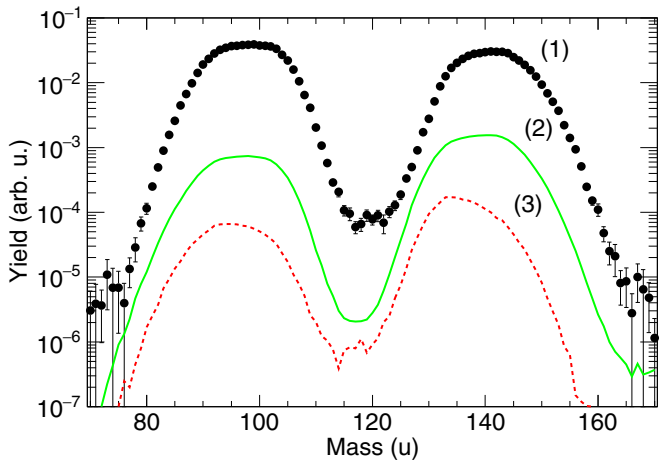

FIG. 7. Fission neutron yield and background components versus fragment mass. The black points (1) represent the measured yield, background due to accidental coincidences is represented by the full green line (2), and the dashed red line (3) represent the neutron yield from the complementary fragment.

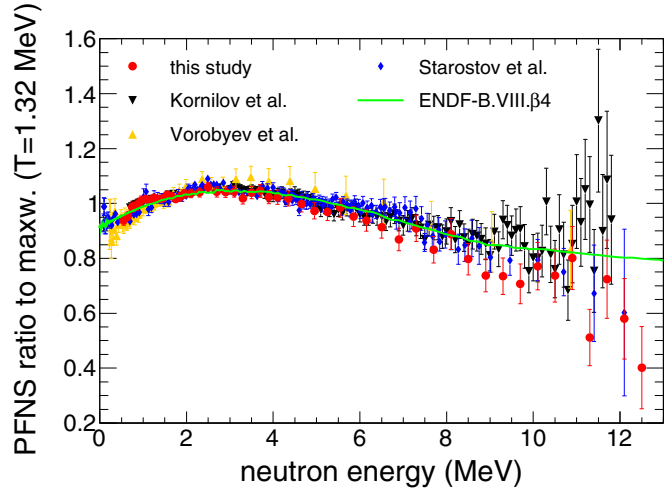

FIG. 8. The laboratory prompt fission neutron spectrum presented as a ratio to a Maxwellian distribution. Data from this study are compared to data from Refs. [33–36] and evaluated data from Ref. [31].

we allowed the spectral shape to depend on the mass number of the primary fragment. Neutrons that are detected with a c.m. angle of emission $\theta_{\text{c.m.}} > 90^\circ$ are not taken into account in this analysis. The effect of ambient background events on each of the observables presented in Sec. III was estimated in a Monte Carlo like fashion, using the fission fragment data without requiring coincidence with the neutron detectors. For each fission event, a false coincidence is generated by randomizing a time of flight, and giving it a weight according to the determined background distribution. The event is then propagated through the analysis as if it were a real event, so that all the same selection criteria are applied. Finally, for each measured distribution a background distribution is obtained that is subtracted from the measured one. The magnitudes of these corrections are shown as a function of fragment mass in Fig. 7. The black points are the efficiency corrected number of recorded neutron coincidences per fission event, the full green line is the background due to accidental coincidences, while the dashed red line is the number of neutrons from the complementary fragment. It is observed that the correction due to complementary fragment neutrons is indeed small, and for most masses negligible. The correction is smaller than 1% over the whole mass region except around 130 u where it reaches a maximum of around 4%. The larger of the two corrections is due to the accidental coincidences with ambient background. The magnitude of this correction is 3.5% of the total number of recorded coincidences. At masses around 80 u and 130 u, where the number of emitted neutrons is small, it reaches about 10% and 20%, respectively.

III. RESULTS AND DISCUSSION

A. Results in the laboratory frame

1. The prompt fission neutron spectrum

The ^{235}U(n, f) PFNS obtained from these data, using the ENDF/B.VII-1 ^{252}Cf(sf) PFNS as reference, is plotted as a ratio to a Maxwellian distribution in Fig. 8. The result from the present study is compared to experimental data on thermal and cold neutron induced fission from Refs. [33–36] and the IAEA evaluation [31]. For the purpose of comparing the shape, all experimental data in Fig. 8, including the data from this study, have been normalized according to the procedure in Ref. [31]. The spectral shape observed in this study, in the incident neutron energy range [0.26 eV, 45 keV], agrees within the uncertainty with experimental data on thermal and cold neutron induced fission. The present result does tend to show a slight softening of the spectrum at high energies compared to the evaluation [31]; this softening is, however, within the estimated experimental uncertainty. The average neutron energy calculated from the present result is $\langle E_n \rangle = (1.99 \pm 0.01)$ MeV, which compares well with the value $\langle E_n \rangle = 2.00$ MeV calculated from the evaluated IAEA standard [31]. To calculate the average neutron energy, the experimental result was fitted with a linear combination of a Maxwellian and a Watt spectrum, the fitted function was used to extrapolate to zero and to 30 MeV.

The ratio of prompt fission neutron spectra from ^{252}Cf(sf) and ^{235}U(n, f) obtained in this study is presented in Table II. A detailed survey of the associated uncertainties is presented in Appendix.

B. Results in the center-of-mass system

1. Neutron spectra in the center-of-mass system

The neutron energy η in the c.m. system has been evaluated on an event-by-event basis, as described in Sec. II C. In Fig. 9 the spectrum integrated over all fragment masses and TKE is displayed. The full red line represents the result of fitting a Maxwellian shape to the data; the resulting temperature is (0.831 ± 0.005) MeV. The integral spectrum deviates from the Maxwellian shape by more than 30% at high energies (above 4.5 MeV) and by about 10% in the low energy range (below 0.75 MeV). The deviation from the Maxwellian shape

TABLE II. Ratio of observed neutron spectra R = PFNS(Cf)/PFNS(U). The average deconvolution correction $\alpha(E)$, as defined by Eq. (8), is given in the third column. The total uncertainty is given in the fourth column and is estimated from the individual components in columns 5–11 assuming that they are uncorrelated. The statistical uncertainties are given in columns 5 and 6 and denoted by Δs_X, where the index X refers to the isotope in question. Columns 7 and 8 are uncertainties related to background corrections, denoted Δb. In columns 9 and 10 uncertainties related to the energy resolution are listed: Δt denotes the uncertainty due to timing resolution and Δl denotes the uncertainty due to resolution in the flight-path length. The last column is an estimate of the uncertainty in the deconvolution correction. See Appendix for details.

E (MeV)	$R(E)$	$\alpha(E)$	ΔR_{tot} ($\times 10^2$)	$\Delta s_{\text{U-235}}$ ($\times 10^2$)	$\Delta s_{\text{Cf-252}}$ ($\times 10^2$)	$\Delta b_{\text{U-235}}$ ($\times 10^2$)	$\Delta b_{\text{Cf-252}}$ ($\times 10^6$)	Δl ($\times 10^2$)	Δt ($\times 10^2$)	$\Delta\alpha$ ($\times 10^2$)
0.55	1.516	0.994	0.53	0.45	0.05	0.17	0.06	0.19	0.06	0.06
0.65	1.504	0.993	0.52	0.44	0.05	0.13	0.04	0.23	0.08	0.06
0.75	1.466	0.993	0.53	0.43	0.05	0.11	0.03	0.26	0.10	0.07
0.85	1.471	0.993	0.56	0.44	0.05	0.10	0.03	0.30	0.12	0.07
0.95	1.461	0.993	0.59	0.45	0.05	0.09	0.03	0.34	0.14	0.07
1.05	1.464	0.993	0.63	0.46	0.05	0.08	0.02	0.37	0.17	0.08
1.15	1.481	0.994	0.66	0.48	0.05	0.07	0.02	0.41	0.19	0.08
1.25	1.483	0.994	0.70	0.49	0.05	0.07	0.02	0.44	0.22	0.08
1.35	1.501	0.994	0.75	0.51	0.05	0.06	0.02	0.48	0.24	0.08
1.45	1.512	0.994	0.79	0.53	0.06	0.06	0.02	0.51	0.27	0.08
1.55	1.505	0.995	0.84	0.54	0.06	0.06	0.02	0.55	0.30	0.08
1.65	1.521	0.995	0.88	0.56	0.06	0.05	0.02	0.58	0.33	0.08
1.75	1.549	0.995	0.93	0.59	0.06	0.05	0.02	0.62	0.36	0.08
1.85	1.547	0.995	0.98	0.61	0.06	0.05	0.02	0.65	0.39	0.08
1.95	1.541	0.996	1.03	0.63	0.07	0.04	0.02	0.69	0.42	0.08
2.10	1.554	0.996	1.00	0.47	0.05	0.04	0.02	0.74	0.47	0.08
2.30	1.569	0.996	1.10	0.51	0.05	0.04	0.02	0.81	0.54	0.07
2.50	1.560	0.996	1.21	0.54	0.06	0.03	0.02	0.88	0.62	0.06
2.70	1.605	0.997	1.32	0.59	0.06	0.03	0.02	0.95	0.69	0.05
2.90	1.622	0.998	1.43	0.64	0.07	0.03	0.02	1.02	0.77	0.03
3.10	1.635	0.999	1.55	0.69	0.07	0.03	0.02	1.09	0.85	0.02
3.30	1.687	0.999	1.68	0.76	0.08	0.03	0.02	1.16	0.93	0.00
3.50	1.667	1.000	1.80	0.82	0.08	0.03	0.02	1.23	1.02	0.03
3.70	1.673	1.000	1.93	0.88	0.09	0.03	0.02	1.30	1.11	0.05
3.90	1.721	1.001	2.07	0.96	0.10	0.03	0.02	1.38	1.20	0.08
4.10	1.734	1.001	2.21	1.04	0.11	0.04	0.03	1.45	1.29	0.11
4.35	1.756	1.002	2.29	0.93	0.09	0.04	0.03	1.53	1.41	0.16
4.65	1.804	1.002	2.51	1.06	0.11	0.04	0.03	1.64	1.56	0.22
4.95	1.868	1.004	2.75	1.21	0.12	0.04	0.04	1.75	1.71	0.30
5.25	1.889	1.008	2.99	1.36	0.13	0.05	0.04	1.85	1.87	0.38
5.55	1.875	1.011	3.24	1.52	0.15	0.05	0.05	1.96	2.04	0.46
5.85	1.957	1.012	3.54	1.74	0.17	0.06	0.06	2.06	2.20	0.57
6.15	2.003	1.014	3.84	1.97	0.19	0.06	0.07	2.17	2.37	0.69
6.50	2.079	1.016	4.08	1.99	0.19	0.07	0.08	2.29	2.58	0.85
6.90	2.200	1.018	4.56	2.39	0.22	0.08	0.10	2.43	2.82	1.08
7.30	2.125	1.021	5.01	2.73	0.26	0.09	0.13	2.57	3.07	1.23
7.70	2.350	1.025	5.68	3.35	0.30	0.11	0.17	2.72	3.33	1.58
8.10	2.224	1.030	6.20	3.79	0.35	0.12	0.22	2.86	3.59	1.72
8.50	2.510	1.035	7.17	4.74	0.41	0.15	0.29	3.00	3.86	2.20
8.90	2.749	1.040	8.21	5.72	0.47	0.18	0.37	3.14	4.13	2.72
9.30	2.796	1.045	9.26	6.75	0.55	0.21	0.48	3.28	4.42	3.10
9.70	2.950	1.052	10.6	8.03	0.63	0.25	0.61	3.42	4.70	3.64
10.10	2.749	1.058	11.4	8.87	0.74	0.28	0.81	3.56	5.00	3.75
10.50	2.918	1.063	13.5	10.9	0.86	0.36	1.04	3.70	5.30	4.38
10.90	2.729	1.068	14.6	12.1	0.99	0.38	1.34	3.84	5.60	4.49
11.30	4.341	1.073	21.3	18.4	1.13	0.72	1.73	3.99	5.91	7.79
11.70	3.115	1.080	20.2	17.7	1.33	0.60	2.31	4.13	6.23	6.06
12.10	3.959	1.086	26.2	23.5	1.52	0.92	2.96	4.27	6.55	8.31
12.50	5.810	1.091	39.3	36.0	1.72	1.61	2.96	4.41	6.88	13.1

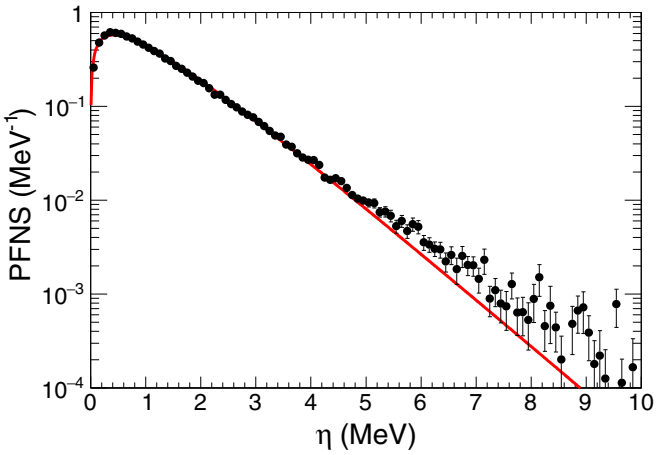

FIG. 9. Integral prompt fission neutron spectrum in the c.m. frame. The full red line represents a Maxwellian spectrum with fitted temperature (0.831 ± 0.005) MeV.

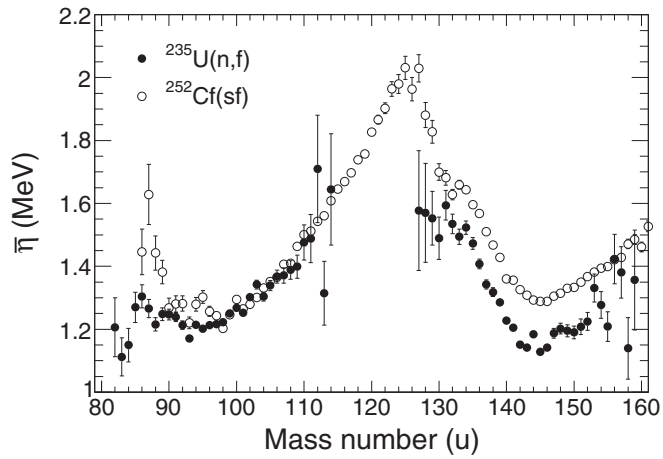

FIG. 11. Average energy of neutrons in the c.m. frame as a function of the fission fragment mass. Data from ^{252}Cf(sf) are included for comparison [32].

at low neutron energies is mainly due to the light fragments. The c.m. neutron spectra for a selection of masses around the most probable light and heavy fragment groups are shown in Fig. 10. While the spectrum of the heavy-fragment group is quite well described by a Maxwellian shape, the spectrum from the light-fragment group is appreciably softer.

The average c.m. neutron energy as a function of the fission fragment mass is shown in Fig. 11. For comparison Fig. 11 also includes data from ^{252}Cf(sf) [32]. Note that the general shape of the mass dependence is approximately the same for the two reactions that produce the fragments. The absolute values are also almost the same for the light fragment group but lower in the case of ^{235}U(n, f) by approximately 150 keV for the heavy fragment group.

2. Average neutron multiplicities

The average neutron multiplicities $\overline{\nu}(A, \mathrm{TKE})$ as a function of fragment mass A and total kinetic energy TKE were calculated from the fission yields $Y(A, \mathrm{TKE})$ and the neutron fragment coincidence spectra transformed to the fragment center-of-mass system as described in the previous section.

The average neutron multiplicity per fragment is shown as a function of the fragment mass in Fig. 12. Averaged over the light and heavy fragment groups, the average number of emitted neutrons are 1.42 and 1.00, respectively. The sawtooth shape of $\overline{\nu}(A)$ can be qualitatively interpreted as a consequence of the interplay of two spherical shell closures: ($Z = 28$, $N = 50$, $A = 78$) and ($Z = 50$, $N = 82$, $A = 132$). When the scission process results in a fragment of mass close to the spherical shell closure, its counterpart will be highly deformed, creating a sawtooth like deformation energy as a function of fragment mass. In low energy fission, the deformation of the nascent fission fragments at scission is the deciding factor for the partition of the total excitation energy and hence the number of emitted neutrons. For comparison, Fig. 12 includes data from Refs. [37,38]; compared to these data sets the present

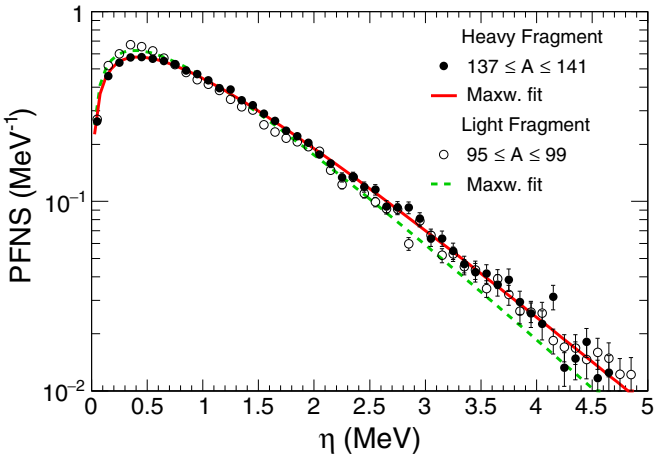

FIG. 10. Prompt fission neutron spectrum in the c.m. frame for selected fission fragment mass ranges around the most probable fragmentation. The full red line and the dashed green line represent best fits of Maxwellian spectra.

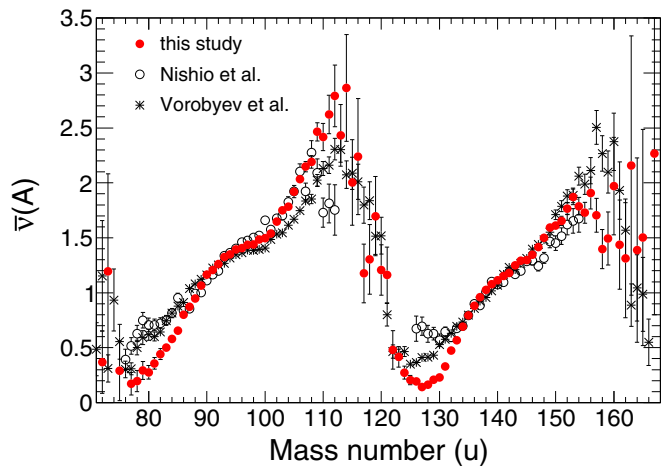

FIG. 12. Average prompt neutron multiplicity per fragment as a function of the fission fragment mass. Data from this study are compared to data from Refs. [37,38].

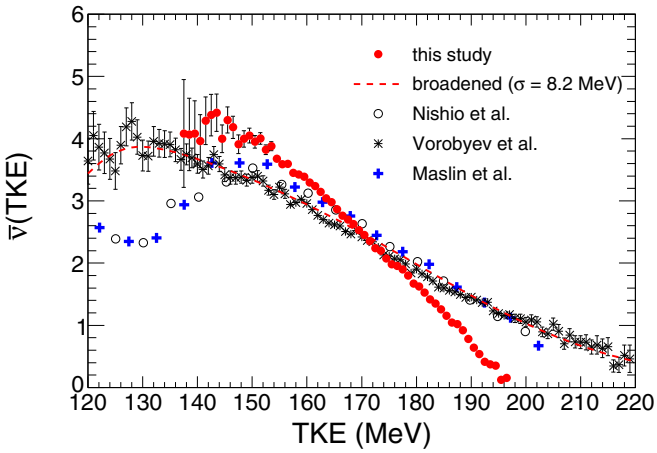

FIG. 13. Average prompt neutron multiplicity per fission as a function of the fission fragment TKE. Data from this study are compared to data from Refs. [37–39].

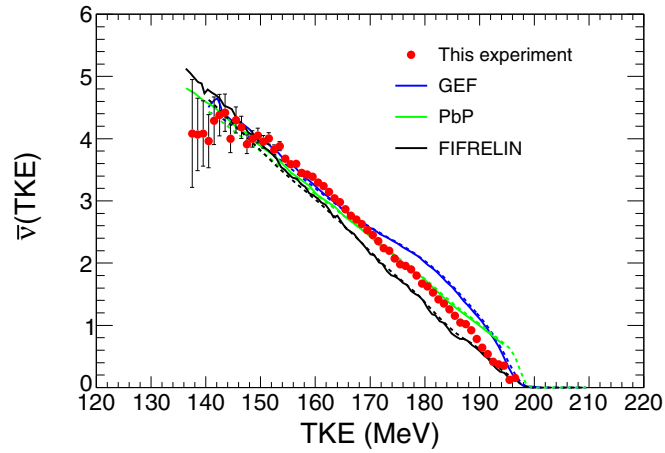

FIG. 14. Average prompt neutron multiplicity per fission as a function of the fission fragment TKE. Data from this study are compared to model calculations, as presented in Ref. [8]. Full lines represent the direct results of the calculation, while dotted lines have been convoluted with the experimental resolution.

measurement shows a more pronounced sawtooth shape, with deeper minima around masses 80 and 130 as well as larger $\overline{\nu}$ in the vicinity of symmetric mass splits. In addition, the shoulders in the region of mass 100 for the light fragment and 140 for the heavy fragments are more pronounced in the present data. The differences with respect to Ref. [38] can be explained by better mass resolution in the present experiment; however, with respect to Ref. [37] the mass resolution is similar. A flattening of the structure is also expected if the random coincidences due to the ambient background are not fully subtracted.

In Fig. 13 the average neutron multiplicity per fission as a function of TKE is compared to data from Refs. [37–39]. As expected from energy balance considerations, a close-to-linear decrease of $\overline{\nu}$ with increasing TKE is observed. A weighted least-square fit results in an inverse slope $-d\,\mathrm{TKE}/d\overline{\nu} = 12.0\ \mathrm{MeV}/n$. This value is substantially lower than the values 16.7–18.5 MeV/n reported in earlier studies of $^{235}\mathrm{U}(n, f)$, performed at thermal incident neutron energies [37–39], but close to the value observed in the spontaneous fission of $^{252}\mathrm{Cf}$. It is also clear, from a visual inspection of Fig. 13, that the present data are in strong disagreement with the literature data. We do not expect that the small increase in the excitation energy of the compound nucleus in this experiment would have a strong influence on this behavior. This expectation is corroborated by comparing the present data to model calculations for thermal neutron induced fission. The five models presented in Ref. [8] agree fairly well with each other; the three with the largest spread are compared with the present data in Fig. 14. It is clear that the model calculations are in much better accordance with the present data than with earlier experiments.

The explanation for the observed discrepancy with earlier experiments becomes apparent when examining the fission fragment TKE distributions from the different studies, as shown in Fig. 15. The distributions from Refs. [37–39] appear broadened. Substantial amounts of yields are found above the maximum available energy 205.87 MeV, as determined by the Q value for the fragmentation, where the heavy fragment is the doubly magic $^{132}\mathrm{Sn}$ nucleus [40]. The dashed line in Fig. 15 represents the result of convolution of the data from this study with a Gaussian resolution function, constructed to reproduce the width of the TKE distributions in the literature data. If the same broadening is applied when determining $\overline{\nu}$(TKE), the dashed line in Fig. 13 is obtained. This qualitatively reproduces features in the literature data, i.e., a less steep slope and $\overline{\nu}$ larger than zero at the maximum available energy.

Kornilov *et al.* have suggested that the observation of $\overline{\nu}$ larger than zero at the maximum available energy is a signature of so-called scission-neutron emission [11]. It was argued that, because evaporation neutrons from the fragments are energetically not allowed at such high TKE, the observed neutrons would have to originate from another source. The difference between experimental data and calculation of $\overline{\nu}$(TKE) based on neutrons evaporated from the fragments was used to estimate the scission-neutron yield. Comparison of the present results with model calculations, as displayed in Fig. 14, shows that no additional source of neutrons is necessary to describe

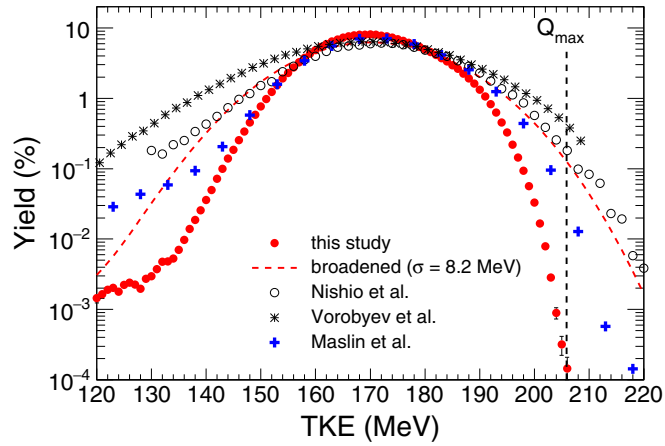

FIG. 15. Fission yield as a function of TKE. Data from this study are compared to data from Refs. [37–39].

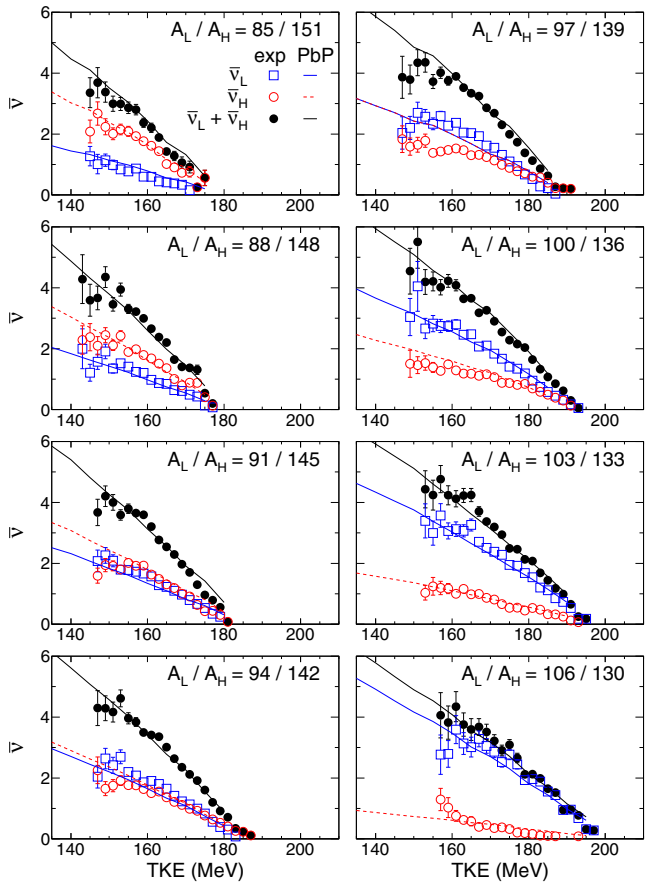

FIG. 16. Average prompt neutron multiplicity as a function of the fission fragment TKE for selected mass pairs, as indicated in the top right corner of each panel. Experimental data for the light, the heavy, and the pair of fragments are compared to point-by-point model calculations [7].

the neutron multiplicity at high TKE. We conclude that the observation of $\overline{\nu}$ larger than zero at the maximum available energy is an experimental artifact, caused by poor TKE resolution. Since all experiments suffers from some resolution broadening, it is important to take this into account when comparison to model calculations are made. In Fig. 14 we have included results obtained by convolution of the model calculations with the estimated TKE resolution of the present experiment. A small effect is visible at high energies where $\overline{\nu}$ approaches zero.

At low TKE the data of Refs. [37,39] show a strong decrease in $\overline{\nu}$; this cannot be explained by the resolution broadening. However, examining Fig. 15, tailings of the TKE distributions can be observed. The tailing is present also in the data from this study, although at much lower intensities compared to the data of Refs. [37,39]. By extrapolating the tailing using an exponential, the relative intensity of the tailing is determined to be larger than 10% for TKE $<$ 140 MeV, while for TKE $>$ 150 MeV the intensity drops below 1%. Events belonging to this tailing are likely due to scattering of the fission fragments in the target foil and/or surrounding materials, as already noted by Maslin *et al.* [39]. The neutron emission from such events, with falsely identified TKE, can be expected to be close to the average value of $\overline{\nu}$. This expectation is consistent with the observed decrease in $\overline{\nu}$ at lower TKE, as the tailing become more and more dominant in the yield.

The varation of $\overline{\nu}$ with TKE for a number of selected mass pairs is shown in Fig. 16. The variation of $\overline{\nu}$ is again nearly linear, except at low TKE. The slope of $\overline{\nu}$(TKE) for a pair of fragments is directly related to the energy necessary to emit a neutron. A slight deviation from linearity is to be expected, since the average neutron separation energy increases with increasing number of emitted neutrons. A structure in the variation of $\overline{\nu}$ with TKE is visible for some mass splits; this shows up as a staircase dependence of $\overline{\nu}$ with lowering TKE. This staircase dependence is a manifestation of the difference in neutron binding energies between mother and daughter nuclei in the neutron-emitting fragments [41]. In Fig. 16 results from the point-by-point model [7] are included for comparison. The average energy cost per neutron entering into these model calculations does take into account the sequential emission of neutrons, responsible for the deviation from a linear behavior with TKE. For the most part the model calculations are in good agreement with the experimental data.

IV. CONCLUSION

A correlation measurement of fission fragments and prompt neutrons emitted in neutron induced fission of ^{235}U was carried out. The measurements were made with a newly developed system consisting of a position-sensitive twin ionization chamber with high detection efficiency for fragment spectroscopy, and an array of proton recoil scintillators for neutron detection. The measurement was carried out at the GELINA neutron time-of-flight facility. The presented results were extracted from the data by summing over the incident neutron energy range [0.26 eV, 45 keV].

The result on the prompt fission neutron spectrum in the laboratory frame is in agreement with the thermal neutron induced fission spectrum, but does tend to show a slight softening at high energies compared to evaluation [31].

The multiplicity and energy of prompt neutrons were obtained as a function of fragment mass and total kinetic energy. The average neutron multiplicity as a function of fragment mass shows a sawtooth shape with more pronounced minima than reported in earlier works. The average neutron multiplicity as a function of TKE shows a slope corresponding to $-d\,\mathrm{TKE}/d\overline{\nu} = 12.0\,\mathrm{MeV}/n$, which is considerably steeper than observed in earlier experimental work, but in agreement with theoretical expectation. The differences with respect to earlier experimental work can be explained by improved fission fragment energy resolution in the present study.

ACKNOWLEDGMENTS

We would like to thank the operators of the GELINA accelerator for providing excellent beam conditions. W. Geerts and C. Bonaldi are also gratefully acknowledged for assistance with technical issues. Beneficial discussions about this work with Prof. A. Tudora as well as Dr. D. Neudecker are also gratefully acknowledged.

APPENDIX: RATIO OF ^{252}Cf(sf) AND ^{235}U(n, f) PFNS AND ASSOCIATED UNCERTAINTIES

The ratio of prompt fission neutron spectra (PFNS) from ^{252}Cf(sf) and ^{235}U(n, f) obtained in this study is presented in Table II. The determination of the associated partial uncertainties is presented in this Appendix.

Background. The uncertainty in the background correction was estimated from the counting statistics of the determined background distribution. The partial uncertainty contribution to the ratio R is denoted ΔB in Table II. Individual uncertainties are given for the ^{235}U(n, f) and ^{252}Cf(sf) measurements. The contribution of the background uncertainty in the ^{252}Cf(sf) measurement is negligible, but is included in Table II for completeness.

Energy resolution. The uncertainty on the PFNS ratio due to energy resolution is calculated according to Ref. [8]. Due to the relative nature of the measurement the uncertainty due to energy resolution is greatly reduced. Using linear error propagation and nonrelativistic approximation of the energy-time relation, the resolution in time of flight σ_t and flight path distance σ_l are transformed to uncertainties in the spectrum ratio:

$$\Delta t^2 = \left(\frac{1}{T_{\mathrm{U}}} - \frac{1}{T_{\mathrm{Cf}}}\right)^2 \frac{8E^3}{m_n l^2}\,\sigma_t^2, \tag{A1}$$

$$\Delta l^2 = \left(\frac{1}{T_{\mathrm{U}}} - \frac{1}{T_{\mathrm{Cf}}}\right)^2 4E^2 \frac{\sigma_l^2}{l^2}, \tag{A2}$$

where m_n is the neutron rest mass and l is the flight path length. The parameters $T_{\mathrm{U}} = 1.32$ MeV and $T_{\mathrm{Cf}} = 1.42$ MeV are temperatures of Maxwellian distributions used as estimates of the spectral shapes for ^{235}U(n, f) and ^{252}Cf(sf), respectively. The resolution in time of flight is given by $\sigma_t = (0.47 \pm 0.05)$ ns, as determined from the width of the prompt γ-ray peak in the time-of-flight spectrum. The resolution in the flight path distance is given by one standard deviation, assuming a uniform detection probability over the length of the neutron detector, as given in Table I. An average detector length of 5.08 cm has been used to arrive at $\sigma_l = 1.47$ cm.

Deconvolution correction. As shown in Fig. 6, the main contribution to the deconvolution correction $\alpha(E)$ is the energy resolution. Since the energy resolution is determined with finite accuracy, it is a source of systematic uncertainty in the correction. We have estimated the contributing uncertainty in the deconvolution correction by

$$\Delta\alpha = \frac{\partial R}{\partial \alpha}\frac{\partial \alpha}{\partial \sigma_t}\Delta\sigma_t. \tag{A3}$$

The partial derivative with respect to σ_t is estimated by calculating correction curves $\alpha(E)$ for varying timing resolutions. A second source of uncertainty is the underlying nuclear data uncertainties in the data library used in the Monte Carlo calculation of the response matrices as well as uncertainties related to sizes and distances between materials in the experimental setup. However, since the differences between a deconvolution correction calculated from the full Monte Carlo model of the setup and one calculated without any material present differs by maximum about 1%, we have neglected these in the uncertainty estimate.

[1] O. Litaize, O. Serot, and L. Berge, Eur. Phys. J. A **51**, 177 (2015).
[2] P. Talou, B. Becker, T. Kawano, M. B. Chadwick, and Y. Danon, Phys. Rev. C **83**, 064612 (2011).
[3] P. Talou, T. Kawano, and I. Stetcu, Los Alamos National Laboratory Technical Report No. LA-CC-13-063, 2013 (unpublished).
[4] K.-H. Schmidt, B. Jurado, C. Amouroux, and C. Schmitt, Nucl. Data Sheets **131**, 107 (2016).
[5] J. M. Verbeke, J. Randrup, and R. Vogt, Comput. Phys. Commun. **191**, 178 (2015).
[6] J. M. Verbeke, J. Randrup, and R. Vogt, Comput. Phys. Commun. **222**, 263 (2018).
[7] A. Tudora and F.-J. Hambsch, Eur. Phys. J. A **53**, 159 (2017).
[8] R. Capote, Y.-J. Chen, F.-J. Hambsch, N. Kornilov, J. Lestone, O. Litaize, B. Morillon, D. Neudecker, S. Oberstedt, T. Ohsawa, N. Otuka, V. Pronyaev, A. Saxena, O. Serot, O. Shcherbakov, N.-C. Shu, D. Smith, P. Talou, A. Trkov, A. Tudora, R. Vogt, and A. Vorobyev, Nucl. Data Sheets **131**, 1 (2016).
[9] P. Talou, R. Vogt, J. Randrup, M. E. Rising, S. A. Pozzi, J. Verbeke, M. T. Andrews, S. D. Clarke, P. Jaffke, M. Jandel, T. Kawano, M. J. Marcath, K. Meierbachtol, L. Nakae, G. Rusev, A. Sood, I. Stetcu, and C. Walker, Eur. Phys. J. A **54**, 9 (2018).
[10] S. Lemaire, P. Talou, T. Kawano, M. B. Chadwick, and D. G. Madland, Phys. Rev. C **72**, 024601 (2005).
[11] N. V. Kornilov, F.-J. Hambsch, and A. S. Vorobyev, Nucl. Phys. A **789**, 55 (2007).
[12] H. R. Bowman, S. G. Thompson, J. C. D. Milton, and W. J. Swiatecki, Phys. Rev. **126**, 2120 (1962).
[13] H. R. Bowman, J. C. D. Milton, S. G. Thompson, and W. J. Swiatecki, Phys. Rev. **129**, 2133 (1963).
[14] C. Budtz-Jørgensen, H.-H. Knitter, C. Straede, F.-J. Hambsch, and R. Vogt, Nucl. Instrum. Methods Phys. Res., Sect. A **258**, 209 (1987).
[15] A. S. Vorobyev, O. A. Shcherbakov, Yu. S. Pleva, A. M. Gagarski, G. V. Val'ski, G. A. Petrov, V. I. Petrova, and T. A. Zavarukhina, Nucl. Instrum. Methods Phys. Res., Sect. A **598**, 795 (2009).
[16] A. Göök, W. Geerts, F.-J. Hambsch, S. Oberstedt, M. Vidali, and S. Zeynalov, Nucl. Instrum. Methods Phys. Res., Sect. A **830**, 366 (2016).
[17] F.-J. Hambsch, J. Van Aarle, and R. Vogt, Nucl. Instrum. Methods Phys. Res., Sect. A **361**, 257 (1995).
[18] P. Geltenbort, F. Gönnenwein, and A. Oed, Radiat. Eff. **93**, 57 (1986).
[19] F. Gönnenwein, in *The Nuclear Fission Process*, edited by C. Wagemans (CRC, Boca Raton, FL, 1991), Chap. 8, pp. 287–473.
[20] C. Wahl, At. Data Nucl. Data Tables **39**, 56 (1988).
[21] H. Nifenecker, C. Signarbieux, R. Babinet, and J. Poitou, in *Proceedings of the Third IAEA Symposium on the Physics and Chemistry of Fission* (IAEA, Vienna, 1973), Vol. 2, p. 117.
[22] A. Gavron, Nucl. Instrum. Methods **115**, 99 (1974).
[23] J. Terrell, Phys. Rev. **127**, 880 (1962).
[24] J. Ziegler, M. Ziegler, and J. Biersack, SRIM computer code, version 2008.04.
[25] P. Talou, T. Kawano, I. Stetcu, J. P. Lestone, E. McKigney, and M. B. Chadwick, Phys. Rev. C **94**, 064613 (2016).

[26] R. Gold, AEC Research and Development Report No. ANL-6984, 1964.
[27] S. Agostinelli, J. Allison, K. Amako, J. Apostolakis, H. Araujo, P. Arce, M. Asai, D. Axen, S. Banerjee, G. Barrand, F. Behner, L. Bellagamba, J. Boudreau, L. Broglia, A. Brunengo, H. Burkhardt, S. Chauvie, J. Chuma, R. Chytracek, G. Cooperman, G. Cosmo *et al.*, Nucl. Instrum. Methods Phys. Res., Sect. A **506**, 250 (2003).
[28] N. V. Kornilov, I. Fabry, S. Oberstedt, and F.-J. Hambsch, Nucl. Instrum. Methods Phys. Res., Sect. A **599**, 226 (2009).
[29] V. V. Verbinski, W. R. Burrus, T. A. Love, W. Zobel, N. W. Hill, and R. Textor, Nucl. Instrum. Methods **65**, 8 (1968).
[30] M. Tajik, N. Ghal-Eh, G. Etaati, and H. Afarideh, Nucl. Instrum. Methods Phys. Res., Sect. A **704**, 104 (2013).
[31] A. Trkov, R. Capote, and V. G. Pronyaev, Nucl. Data Sheets **123**, 8 (2015).
[32] A. Göök, F.-J. Hambsch, and M. Vidali, Phys. Rev. C **90**, 064611 (2014).
[33] N. V. Kornilov, F.-J. Hambsch, I. Fabry, S. Oberstedt, T. Belgya, Z. Kis, L. Szentmiklosi, and S. Simakov, Nucl. Sci. Eng. **165**, 117 (2010).
[34] V. N. Nefedov, B. I. Starostov, and A. A. Boytsov, IAEA Report INDC(CPP)-0457 (2014), English translation from 6-th All-Union Conf. on Neutron Physics, Kiev, Vol. 2, p. 285 (1983), EXFOR entries 40871011,40871012.
[35] B. I. Starostov, V. N. Nefedov, and A. A. Boytsov, IAEA Report INDC(CPP)-0458 (2014), English translation from 6-th All-Union Conf. on Neutron Physics, Kiev, Vol. 2, p. 290 (1983), EXFOR entry 40872007.
[36] A. S. Vorobyev and O. A. Shcherbakov, IAEA report INDC(CCP)-0455, English translation of selected papers published in Voprosy Atomhnoj Nauki i Tekniki, Series: Yadernye Konstanty (Nuclear Constants), Issue No. 1-2 (2011–2012).
[37] K. Nishio, Y. Nakagome, H. Yamamoto, and I. Kimura, Nucl. Phys. A **632**, 540 (1998).
[38] A. S. Vorobyev, O. A. Shcherbakov, A. M. Gagarski, G. V. Val'ski, and G. A. Petrov, EPJ Web Conf. **8**, 03004 (2010).
[39] E. E. Maslin, A. L. Rodgers, and W. G. F. Core, Phys. Rev. **164**, 1520 (1967).
[40] M. Wang, G. Audi, A. Wapstra, F. Kondev, M. MacCormick, X. Xu, and B. Pfeiffer, Chin. Phys. C **36**, 1603 (2012).
[41] O. Litaize, O. Serot, L. Thulliez, and A. Chebboubi, EPJ Web Conf. **146**, 04006 (2017).